From the graph we can see that after α = 23° the momentum is negative, we must avoid this condition.

Hydrodynamic analysis

In this analysis the hull was studied using a regular wave of amplitude 1 m and the period has changed from 2s to 12s.

Two tests were carried out with ANSYS AQWA, one with an incident wave in the longitudinal direction with respect to the hull and another in a transversal direction. The individual tests were carried out with different forward speed values.

Longitudinal incident wave: results

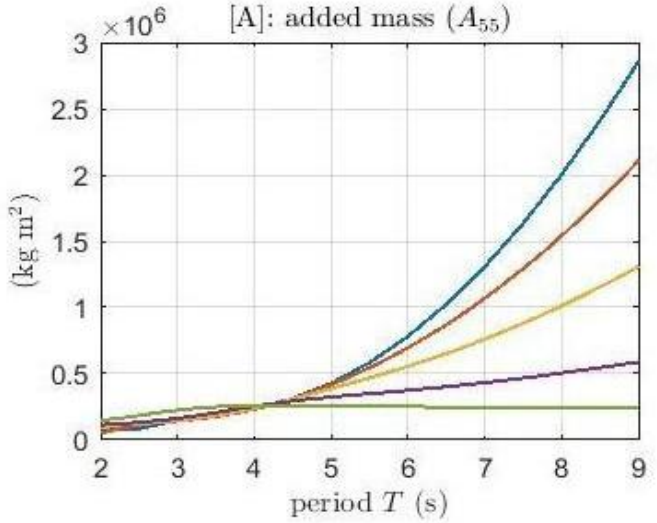

Figure 8: Added mass in pitching degree

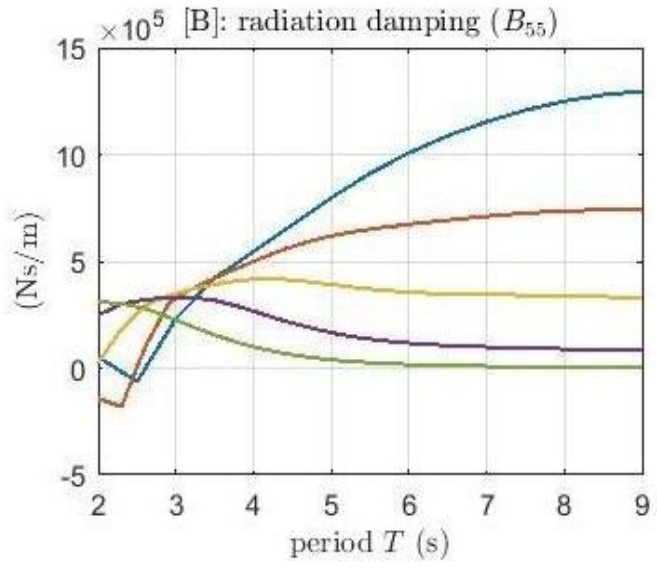

Figure 9: Damping in pitching degree

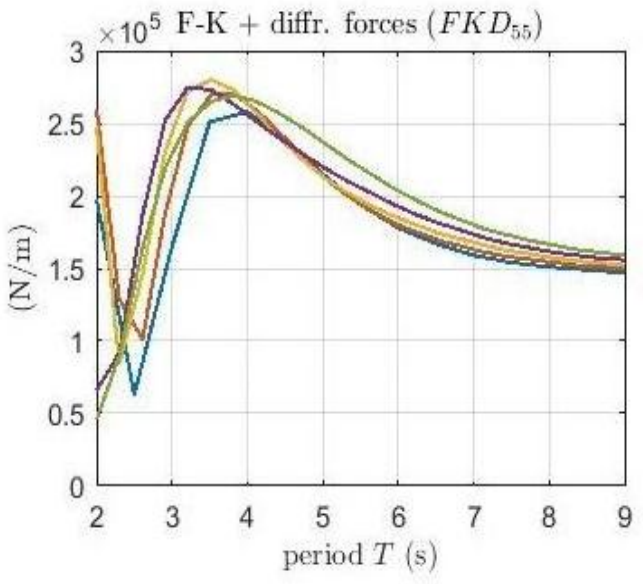

Figure 10: Froude - Krylov and Diffraction forces in pitching degree

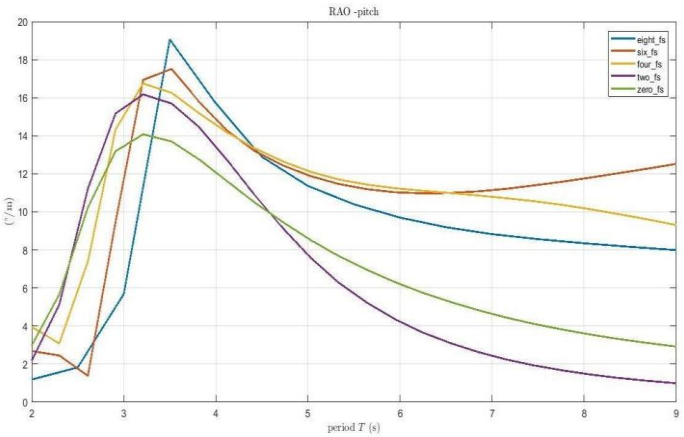

Figure 11: RAO in pitching motion

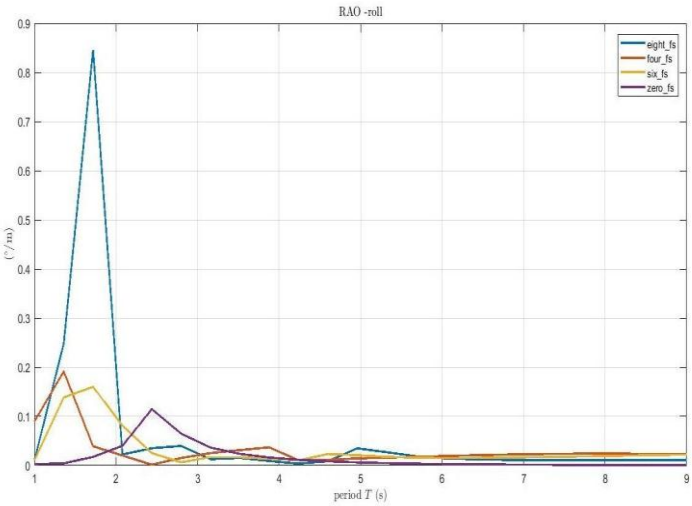

Figure 12: RAO in roll motion

Considerations

The *added mass* can be seen as the added mass of water, which is carried by the hull in its motion. Instead, damping corresponds to the energy that is sent in the far field (*radiated energy*). These two contributions make up the *radiation force*. They are constituted by two matrices 6x6 where on the diagonals there are the calculated elements by ANSYS AQWA, for each translations (surge, sway, heave) and rotations (roll, pitch, yaw). Since we are considering an *incident longitudinal wave* to the hull, we will analyse the *pitching degree of freedom* so we will take account only the A_{55} coefficient of the added mass matrix and B_{55} coefficient of damping matrix.

Another important premise that must be made is that these tests are carried out with different forward speed of the hull and since the numerical evaluation of the translating – pulsating Green's function is very time consuming, the experience suggest us to maintain a value of Froude number <0,3. From this observation, applying the inverse formula:

$$v = F_n\sqrt{gL}$$

Where:

- Fn is the Froude number = 0.3
- g is the gravitational acceleration
- L is the length of the hull

Is possible to obtain the maximum velocity (3,6 m/s) beyond which the results could present some errors.

Analysing the graph of the added mass, A_{55}, we can see that with waves characterized by a relatively small period (until 4.2 s) the effect of the change in the forward speed is indifferent because, as we can see, the value of added mass is almost constant. Instead with waves characterized by a higher period (over 4.2 s) the forward speed of the hull has an increasingly incisive value. This is closely linked to the concept of *hydrodynamic resistance*. We get the maximum added mass value with the maximum forward speed (8 m/s) because higher is the hull's speed, higher would be the hydrodynamic resistance and so, consequently, the adhesion condition of the fluid particles on the hull will be more incisive (i.e. the hull will carry with itself more mass).

Then analysing the radiation damping graph, B_{55}, we can see that as the incident wave and the forward speed of the hull increase, the radiation damping assumes higher and higher values. This means that the relative speed between wet body and water is high; consequently, there is a strong dissipation of energy because the hull cannot follow perfectly the path of the wave.

From the graph, we can see that the effect of forward speed on the excitation forces is indifferent because all the curves maintain almost the same values and trends. A peak is recorded at about 3.5 s of period, at the same point where the RAO is maximum. This means that the rotations of the hull around the y-axis (pitch) are elevated as a consequence higher will be the generation of diffracted waves that run off from the hull to the far field (increase in diffraction forces). Furthermore, this wave motion generates a greater hydrostatic pressure than that which we would have in still water (increase of the forces of Froude - Krilov).

Then analysing the graph of the RAO (in pitching motion), figure 11, we can observe that as the forward speed increases, the RAO tends asymptotically (for high wave periods) to higher values. The relative speed between wet vehicle and water increases with increasing forward speed. Then positioning on the hull reference system, the wave period decreases because the hull is moving forward. Consequently, since the wave period becomes smaller, the value of the RAO will be greater (because for smaller wave periods we get closer to the value of the *resonance frequency*) to large values of periods of the incident wave. Generally the RAO may have a peak corresponding to an intermediate wave period due to the low damping factor [2]. On the other hand, the RAO graph in roll motion, in figure 12, shows a wave peak with a shorter period, precisely at 1.5s. This respects the empirical law that suggest us that the length of the hull must be almost 1/3 of λ. In this case, we are considering the transversal length of the vessel that is smaller than the longitudinal length so the hull reaches the resonance frequency to smaller periods of the wave.

GYROSCOPE SYSTEM

The figure below shows the three main components of the gyroscopic system: the flywheel (red), the gyro – structure (blue), the PTO (green). To describe the system dynamics three reference frames have to be introduced:

- The fixed reference axes (FRA) is the inertial one and its axes are x_0, y_0, z_0.
- The hull – fixed coordinate system (LSA) is composed by x_1, y_1, z_1.
- The gyroscope structure fixed coordinate system (GSA) is composed by x_2, y_2, z_2.

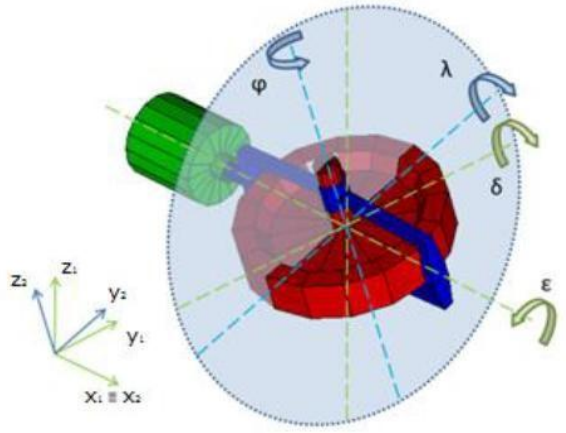

Figure 13: Gyroscope system reference frame.

The combination of the pitch speed $\dot{\delta}$ with the flywheel speed $\dot{\varphi}$ about the z_2 axis generates a gyroscope torque T_ε around the $x_2 \equiv x_1$ axis, which can be exploited by the PTO for power

conversion. So that the gyroscopic moment is given by the cross product of the pitch speed $\dot{\delta}$ along y_1 by the flywheel angular momentum L along z_2 thus the resulting torque is T_ε along the x_1 axis

$$T_\varepsilon \overrightarrow{i_2} = \dot{\delta}\overrightarrow{j_2} \times L\overrightarrow{k_2}$$

The choice of the vacuum system have a justified reason: the viscous forces acting on the surface of the flywheel depend on the rotation speed and pressure around the flywheel. For the ISWEC system it was estimated that reducing the value from 1 bar to 0.01 bar the aerodynamic drag force is reduced of 80 – 90%. The graph evidences the magnitude of the power losses due to the aerodynamic viscous forces depending on different value of internal chamber pressure.

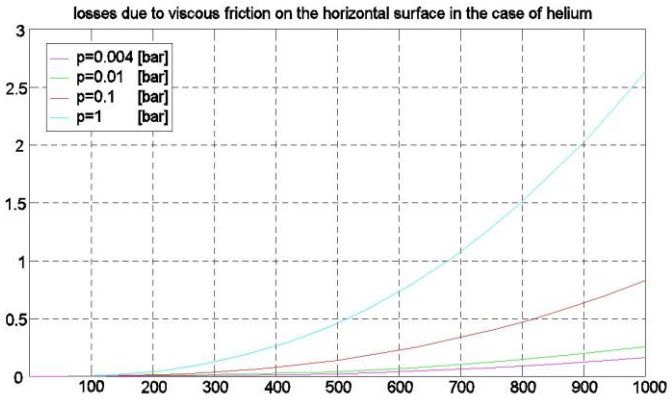

Figure 14: Aerodynamic drag actingon the ISWEC flywheel as a function of the chamber pressure

Adjustment of the flywheel angular velocity with respect to the sea state is another a very important factor that affects the productivity of the system. This is demonstrated by the following graph, which is referred to the ISWEC system, from which emerges that keeping a constant speed of the rotating disk will produce an annual production of electricity lower than that considered with an adaptation of the angular velocity of the flywheel [17].

Power losses on the gyroscopic system

When scaling a system, productivity and the respective power losses vary with the scale factor. In this paragraph a mathematical formulation has been reported that allows us to calculate the power losses based on the scale factor that has been used.

The mechanical power losses on the flywheel spinning axis can be identified as follow[18]:

$$P_{losses} = P_v + P_{bear} + P_{seal} \quad (14)$$

Where:

- P_v are the power losses due to the aerodynamics forces;
- P_{bear} are the power losses carried by the flywheel roller bearings;
- P_{seal} are the power losses provided by seals friction forces.

Fluid – dynamic power losses

The fluid – dynamic losses arise from the interaction between the flywheel surface and air. These power losses depending on both the fluid speed regime (laminar or turbulent) and the spaces between the flywheel and the vacuum chamber. In the vacuum chamber there are two meatus (figure) identified as -s- and -m- the interaction between the air that fills these meatus and the flywheel surface leads to two different power losses contributes[18]:

$$P_v = P_{v,lateral} + P_{v,disk} \quad (15)$$

Where:

- $P_{v,lateral}$ refers to the lateral meatus (m);
- $P_{v,disk}$ refers to the top and bottom meatus (s)

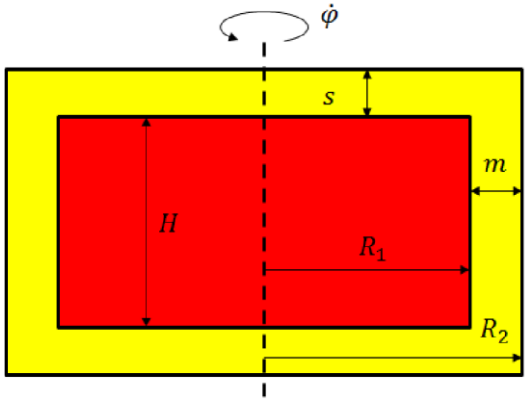

Figure 15: Flywheel and vacuum chamber scheme

Starting from the lateral meatus, the mathematical expression of $P_{v,lateral}$ is:

$$P_{v,lateral} = \frac{1}{2} C_M \cdot \pi \cdot \rho_{air} \cdot \dot{\varphi}^3 \cdot R_1^4 \cdot H \quad (16)$$

Where:

- C_M is the torque coefficient;
- $\dot{\varphi}$ is the flywheel speed;
- R_1 is the external diameter of the flywheel;
- H is the height of the flywheel;

For what concern the top and bottom meatus, the power loss carried by the air friction on the top and bottom surfaces of the flywheel can be determined as follow:

$$P_{v,disk} = 2 \cdot (\frac{1}{2} \cdot C_M \cdot \pi \cdot \rho_{air} \cdot \dot{\varphi}^3 \cdot R_1^5) \quad (17)$$

Both these expressions depend on the Reynolds number of the speed regime.

The mathematical expressions of power losses carried by the air inside the vacuum chamber depend on several parameters such as geometrical features (R_1,m,H), flywheel speed and air thermodynamic conditions (ρ_{air},μ_{air}). Each of these terms have a different influence on P_v: taking into account the most important contributes on power losses, it is possible to design both the flywheel and vacuum chamber in order to avoid high

dissipations. More in details, the influence of the flywheel speed depends on the speed regime: passing from a low turbulent speed regime to a high turbulent speed regime results in a higher exponent on the flywheel speed for both $P_{v,lateral}$ and $P_{v,disk}$ [18].

Bearing power losses

Once calculated the forces acting on bearings, the mathematical expression of the power losses for both axial and radial loads can be determined according to the simplified SKF friction moment formulation:

$$P_{bear,rad} = \frac{1}{2}\mu_{bear} \cdot F_{rad} \cdot d_{bear} \cdot \dot{\varphi} = \frac{1}{2L}\mu_{bear} J \cdot \dot{\varphi} \cdot \dot{\varphi} \cdot \dot{\varepsilon} \cdot d_{bear} \quad (18)$$

$$P_{bear,ax} = g \cdot \mu_{bear} m_v \cdot d_{bear} \cdot \dot{\varphi} \quad (19)$$

The radial power losses depend both on the flywheel rotational speed and flywheel inertia and thus on the angular momentum ($L = J \cdot \dot{\varphi}$). On the other hand, the axial power losses depend only on the flywheel speed and flywheel mass. It has been demonstrated that the higher contribute of the power losses provided by bearing is given by the radial forces, so the gyroscopic reaction on the flywheel shaft T_λ, should be limited acting on the flywheel inertia or on its speed[18].

Seal power losses

The last source of power losses is due to the seals: in order to maintain the vacuum insiede the flywheel chamber and to prevent oil leakages, two seals are used. The mathematical relation of the seals power loss is:

$$P_{seal} = F_r \cdot \pi \cdot \frac{d_{seal}^2}{2} \cdot \dot{\varphi} \quad (20)$$

Where:

- F_r is the friction force per unit of length on the surface contact between the seal and the flywheel shaft;
- d_{seal} is the seal diameter.

Taking into account the F_r, it depends on the pressure difference between the air inside and outside the chamber and on the seal material. The graph below shows the friction force of the seals of the ISWEC full – scale. Interpolating the red curve selecting a proper number of points allows obtaining the mathematical expression of the friction force:

$$F_r = 67\frac{N}{m} + 201.3\frac{N}{m \cdot MPa^{0.6}} \cdot \Delta p^{0.6} \quad (21)$$

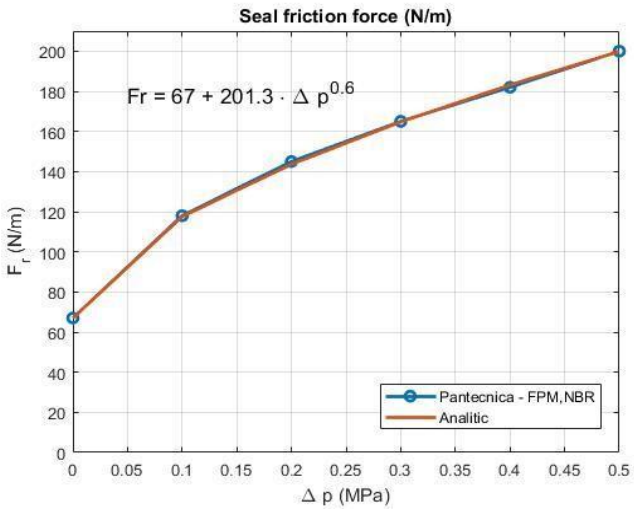

Figure 16: Friction force on seal surface in function of pressure difference on it

Substituting the equation (21) in (20) the mathematical expression of the seal power losses becomes[18]:

$$P_{seal} = \frac{\pi}{2}(67 + 201.3\Delta p^{0.6}) \cdot d_{seal}^2 \cdot \dot{\varphi}$$

Referring to the relations above defined the appropriate power losses scale factors have been obtained. Froude theory has been used for scaling.

It is worth pointing out that almost all the exponents of the power losses scale factors are smaller than the scale factor of the extracted power ($\lambda^{\frac{7}{2}}$). This allows concluding that the power losses grow with a smaller rate that the extracted power, as the scale factor increases.

Trends of scaled power losses

A numerical example aims to quantify the power losses with respect to the extracted power of the device and to evaluate the effect of the scale factor on the system efficiency.

The kinematic parameter has been defined, considering the experimental hull and gyroscope speed in correspondence of a wave having energetic period equal to 5s and a significant height equal to 1.14m, as well as the flywheel spinning velocity (full – scale device experimental data acquired on 7 October 2015)[18]:

From the graph, we can see that the power losses decrease with a reducing scale of the model. The important losses on the flywheel shaft are carried by the seal, followed by the radial bearing losses and fluid – dynamics losses and then by the axial bearing losses [18].

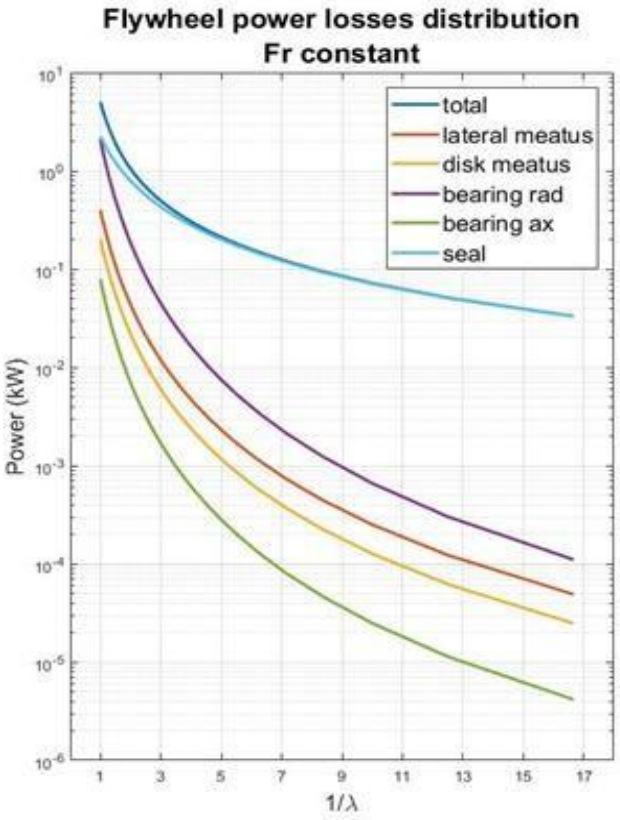

Figure 17: Flywheel power losses on ISWEC

CONCLUSIONS

The *hydrostatic study* of the hull has led to the creation of a graph (figure 7) from which it is possible to evaluate that after a certain inclination of the hull (α = 65 °), the moment, applied by the hydrostatic thrust that acts on the wet surface of the hull, is no longer *righting* but becomes *heeling*. Instead, through the *hydrodynamic study* of the boat it was possible to evaluate the maximum pitching degree with different forward speed in the case of an incident wave in the longitudinal direction to the hull. The values obtained, for the various forward speed, all record a peak in the period of the wave of 3.5s reaching a maximum value of RAO (figure 11) equal to 19°, with a forward speed equal to 8 m/s. Instead, looking at the RAO - roll graph (figure 12), we can see that the inclinations due to the rolling movement are very low if the hull is hit by a longitudinal wave, so this type of wave does not affect the rolling motion at all. Therefore, we get the resonance frequency of the system for an incident wave of period equal to 3.5s and probably we will get the maximum productivity of the system with this wave period value. This is due to the fact that through the value of pitch angle is possible to calculate the momentum that is created around the precession axis of the gyroscope, which will then be transformed by the PTO into electric energy, so higher is the pitch angle, higher would be the pitching speed, greater would be the productivity of the. The same applies to the angular momentum (L) created by the rotation of the flywheel around its axis: with higher values of L, more electrical energy could be harvest in the system. This is the main reason why the design of the 1:7 scale prototype started respecting geometric constraints (external diameter of the flywheel, flywheel height, inter-axis between the bearings), because precisely these contribute to an increase in angular momentum, hence in the productivity of the system.

The study shows that, from an analytical point of view the speed and the external radius of the flywheel play an important role in the flywheel power losses magnitude. More in details, the flywheel speed appears in all the relations of the power losses representing the most important contributions to the dissipated power. Thus, one of the main steps in design process of a gyroscopic system is the choice of the angular momentum ($L = J \cdot \dot{\varphi}$) that is the physical quantity involved into the power extraction: make a correct balance between the flywheel inertia (J) and the flywheel speed ($\dot{\varphi}$) will allow limiting the power losses.

REFERENCES

[1] Falcão, António FO. "Modelling of wave energy conversion." Instituto Superior Técnico, Universidade Técnica de Lisboa (2013).

[2] A.F. de O. Falcão, Wave energy utilization: a review of the technologies, Renewable and Sustainable Energy Reviews, 14 (3) (2010), pp. 899–918.

[3] Iraide López, Jon Andreu, Salvador Ceballos, Iñigo Martínez de Alegría, Iñigo Kortabarria, Review of wave energy technologies and the necessary power-equipment, Renewable and Sustainable Energy Reviews, Volume 27, November 2013, Pages 413-434, ISSN 1364-0321, http://dx.doi.org/10.1016/j.rser. 2013.07.009.

[4] Güney, Mükrimin Şevket. "WAVE ENERGY CONVERSION SYSTEMS." Deniz Bilimleri ve Mühendisliği Dergisi 11.2 (2015).

[5] EU Horizon 2020, "Secure, Clean and Efficient Energy", https://ec.europa.eu/programmes/horizon2020/en/h2020-section/secure-clean-and-efficient-energy, accessed May 2016.

[6] US Department of Energy "Marine and Hydrokinetic Market Acceleration and Deployment", http://energy.gov/eere/water/marine-and-hydrokinetic-market-acceleration-and-deployment#ad, accessed May 2016.

[7] WATERLAS, "Wind and Wave Atlas of the Mediterranean Sea Wind and Wave Atlas of the Mediterranean Sea," 2004.

[8] M. T. Pontes, R. Aguiar, and H. Oliveira Pires, "A Nearshore Wave Energy Atlas for Portugal," *J. Offshore Mech. Arct. Eng.*, vol. 127, no. 3, p. 249, Aug. 2005.

[9] BOEM (bureau of Ocean Energy Management), "Ocean Wave Energy | BOEM," 2007. [Online]. Available: https://www.boem.gov/Ocean-Wave-Energy/. [Accessed: 03-Mar2018].

[10] Bracco G., "ISWEC: a Gyroscopic Wave Energy Converter," 2010.

[11] *Cummins W. E.*, 1962: The impulse response function and ship motions, David Taylor model basin, report 1661, Department of the Navy, Washington DC.

[12] *Ansys*, 2012: Ansys AQWA User Manual

[13] *WAMIT*, 2015: WAMIT User Manual

[14] *Airy, G. B.*, 1841 Tides and Waves

[15] ANSYS Inc., "Aqwa Theory Manual," *Ansys*, vol. 15317, no. January, p. 174, 2013.

[16] D. Skandali, "Identification of response amplitude operators for ships based on full scale measurements," *Tech. Univ. Delft*, no. September, 2015.

[17] M. Raffero, "Design of a Wave Energy Converter-A case of application: ISWEC," 2014.

[18] N. Pozzi, V. Calamusa, and M. Bonfanti, "Power losses on iswec," *Paper*, 2017.